Mineralium Deposita (2023) 58:1477–1497
https://doi.org/10.1007/s00126-023-01189-5

ARTICLE

Petrogenesis of the Mesoarchaean Stella layered intrusion, South Africa: implications for the origin of PGE reefs in the upper portion of layered intrusions

Wolfgang D Maier[1] · Sarah-Jane Barnes[2] · William D Smith[3]

Received: 5 May 2022 / Accepted: 13 June 2023 / Published online: 12 July 2023
© The Author(s) 2023

Abstract
The ~3033 Ma Stella layered intrusion is hosted by supracrustal rocks of the Kraaipan–Madibe greenstone terrane, South Africa. The studied portion of the intrusion consists mainly of magnetite leucogabbro and magnetite anorthosite, as well as several massive magnetite layers. The intrusion hosts a laterally continuous, ~60-m-thick, PGE mineralized interval, with total resources amounting to 108t Pt + Pd + Au, constituting one of the oldest known PGE reef-style mineralizations on Earth. The richest reef, with a grade of 4.4 ppm Pt+Pd over a width of 5–8 m, occurs in semi-massive magnetitite. It is suggested that the mineralized oxide and silicate layers formed through a combination of primary magmatic, late magmatic, and hydrothermal processes, including granular flow and phase sorting of a magnetite- and sulfide-bearing gabbroic crystal mush that crystallized from a tholeiitic basalt, as well as remobilization of S and metals by late magmatic and hydrothermal fluids that led to crystallization of platinum-group minerals.

Keywords Layered intrusion · South Africa · Platinum-group elements · Platinum-group minerals · Archaean · Ore deposit

Introduction

Platinum-group elements (PGE) are critical metals required in the production of catalytic converters and fuel cells. However, apart from extensions and development of existing ore bodies, largely in the Bushveld Complex of South Africa and at Noril'sk, Russia, few new economically viable PGE deposits have been found in the last decades. Thus, the world's primary PGE production remains centered on the Bushveld Complex and Noril'sk, with smaller contributions from the Great Dyke of Zimbabwe, the Stillwater Complex, USA, and the Lac des Iles intrusion of Canada. The Stella layered intrusion of South Africa (Fig. 1) is interesting in this regard because its mineralized reefs are among the oldest on Earth and occur in an unusual stratigraphic position, i.e., within the upper, relatively evolved portion of the intrusion. This has opened new search spaces for PGE exploration (Maier et al. 2003). In this paper, we present a detailed petrological study of the mineralized interval and propose a refined ore model.

History of exploration, regional geology, and tectonic setting

The Stella intrusion is located in the Northwest Province of South Africa, ~400 km to the west of Pretoria (Fig. 1). The name "Stella" derives from a comet that was visible in the skies in the 1880s (Theal 1919). The intrusion has been dated at 3033.5 ± 0.3 Ma (Schmitz et al. 2004). It is hosted by the western (Stella) limb of the poorly exposed Kraaipan–Madibe greenstone terrane, which also includes the Goldridge, Madibe, and Amalia belts (Ramotoroko et al. 2016). The Kraaipan-Madibe terrane comprises a diverse range of lithologies. In addition to mafic volcanics in the greenstone belts, there are quartzites and banded iron formations (3410 + 61–64 Ma; Anhaeusser and Walraven

Editorial handling: M. Fiorentini

✉ Wolfgang D Maier
maierw@cardiff.ac.uk

[1] School of Earth and Environmental Sciences, Cardiff University, Cardiff, UK

[2] Sciences de la Terre, Université du Québec à Chicoutimi, Chicoutimi G7H 2B1, Saguenay, Canada

[3] Department of Earth Sciences, Carleton University, Herzberg Laboratories, Ottawa, Ontario K1S 5B6, Canada

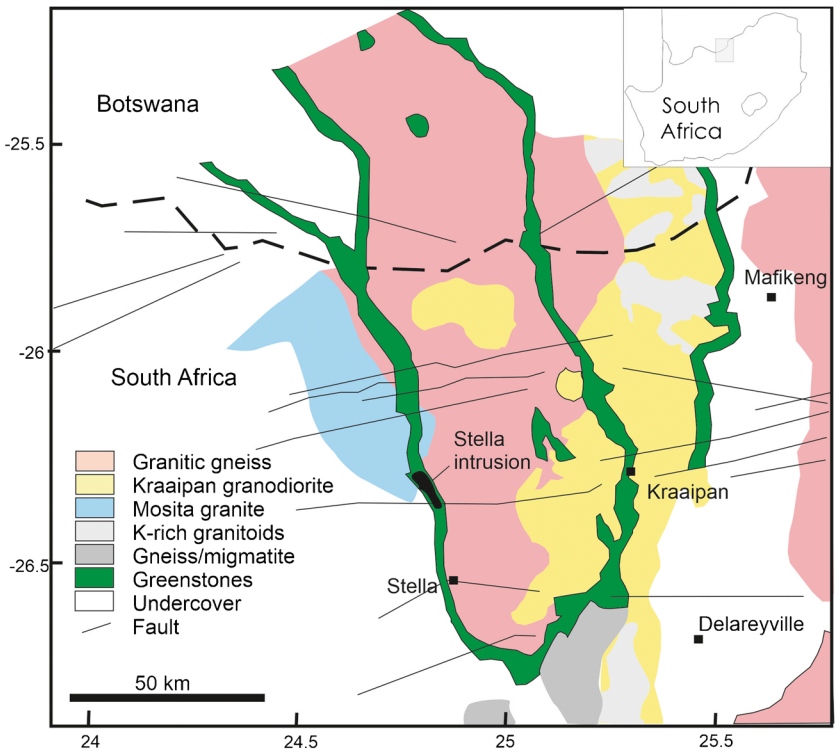

Fig. 1 Geology of the Kraaipan–Madibe greenstone terrane hosting the Stella intrusion (modified after Ramotoroko et al. 2016)

1999), felsic intrusive rocks including tonalite and trondhjemite forming the regional basement (3162 to 3070 Ma, Anhaeusser and Walraven 1999), as well as post-tectonic rhyolite (2914 Ma, M. de Wit pers. com. to H. Jelsma) and K-rich granodiorite and adamellite (2880 to 2846 Ma) (Fig. 1).

Geology of the Stella intrusion

The Stella intrusion was originally delineated in the early 1970s by means of aeromagnetic surveys and drilling which established a strike extent of ~13 km and an estimated stratigraphic thickness of ~1.5 km (ESM 1a). The intrusion is thought to represent the upper portion of an originally larger and thicker, but tectonically dismembered, layered intrusion (Andrews 2002). Two sections have been delineated, Morester in the North and Kroomdraai in the South, both being ~6 km long. Several PGE-rich deposits have been delineated by drilling, including Crater and Sirius in the Morester section, and Orion and Crux in the Kromdraai section. Deformation resulted in west over east, bedding parallel, ductile, in places mylonitic, shearing and thrusting, particularly at the contact between competent and less competent lithologies, e.g., magnetitite and diabase dykes. The widths of the shear zones can be up to 2 m. Late brittle reverse faulting caused conjugate fault sets, trending 010–040° and 100–115°, and compartmentalization of the intrusion, with up to ~50 m horizonal displacement (ESM 1b), and unknown vertical displacement. This led to local duplication of the reef, resulting in thickening to as much as 70 m (at the Crux deposit, ESM 1a).

The basal contact of the intrusion is not exposed at the surface. In drill core, the contact zone consists of intercalated magnetite–quartz schist, chert, and highly altered intrusive rocks, displaying abundant quartz veining. The contact zone is overlain by medium- to coarse-grained leucogabbro, magnetite leucogabbro and anorthosite, hosting more than 10 magnetitite layers, 0.4–4 m thick. Contacts between layers are mostly gradational (Fig. 2). The layers dip broadly sub-vertically or are locally overturned with a westerly dip, but there are strong variations on a local scale due to faulting and folding.

In the present study, borehole intersection W955D was examined in detail (ESM 2a). The borehole plunges at ~45° to the east. The foliation of plagioclase grains in the drill core suggests that the bore hole intersected the reef interval at an angle of ~45° (Fig. 2). This could suggest that the true thickness of the ~250-m mineralized interval, including the 1.8-m-thick main mineralized magnetitite, is reduced by a factor of 0.71.

The uppermost 40m of the drill core, representing the stratigraphic base of the examined sequence, consist largely of magnetite-poor leucogabbro that is locally pegmatitic (Fig. 3, ESM 1c). This is underlain by ~50 m of leucogabbro containing 1–15 modal % magnetite. In most rocks from ~90 to 220 m, the magnetite content of leucogabbro is > 15%, and numerous massive (> 50 wt.% oxide) to semi-massive (20–50

Fig. 2 Drill core W955D intersecting upper main reef magnetitite and magnetite leucogabbro as well as a diabase dyke. Note sample S19 (~15ppm PGE) collected from 201.1-201.3m.

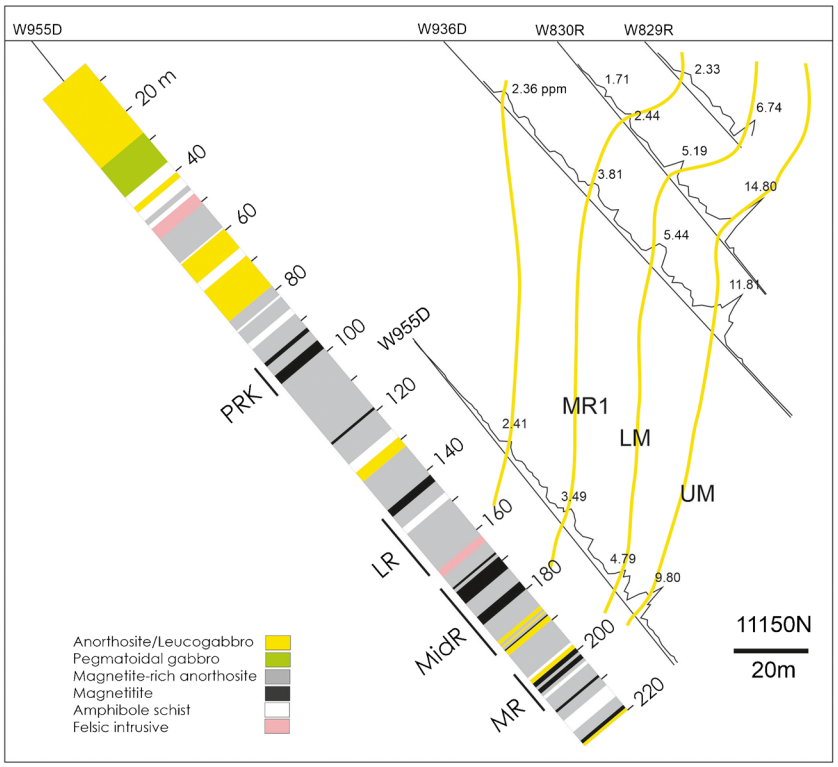

Fig. 3 Concentrations of Pt+Pd+Au in drill cores at Stella (drill line 11150N). Numbers next to log of bore hole W955D denote depth of drill core in meters. Figure modified after Andrews (2002)

wt.% oxide) magnetite layers occur. The rocks are mostly medium- to coarse-grained, or locally pegmatitic, consisting of euhedral and subhedral plagioclase now replaced by amphibole and chlorite, and interstitial magnetite.

There are a number of different felsic rock types present in the drill cores, including oligoclase–quartz rocks containing xenoliths of the host leucogabbro and showing strongly sheared contacts with the host rocks, implying they are pre- to syn-tectonic. Abundant fine-grained quartz–albite veins oriented sub-parallel to the igneous layering have thicknesses of centimeters to 10s of meters. Many display chilled margins and are unaltered and undeformed, suggesting they formed after the deformation of the leucogabbro. Coarse- to medium-grained granite veins are less common than the quartz–albite veins and measure up to a few m in thickness. They consist of plagioclase, quartz, alkali feldspar, locally biotite and myrmekite and contain blocks of sheared gabbro indicating that the veins are post-tectonic in age.

There are two distinct sets of mafic dykes: diabase of Fe-rich tholeiitic composition is oriented predominantly sub-parallel to the igneous layering and has been altered to amphibole schist consisting of actinolite, chlorite, quartz,

plagioclase, and epidote. These dykes are less altered and deformed than the Stella cumulates but have mostly sheared contacts with the cumulates and thus likely intruded during the late stages of tectonism (Fig. 2). MELTS simulations (rhyolite MELTS v 1.2.0) yielded a crystallization sequence and mineral compositions matching the Stella cumulates suggesting the dykes could represent the parent magmas to the Stella intrusion. A second suite of mafic dykes trends ENE and is clearly visible on aeromagnetic maps (ESM 1a). These magnetite gabbros dykes have chilled margins and brecciated contact zones.

Some boreholes intersected up to 200 m of diamictite likely belonging to the Kameeldoorn Formation of the Ventersdorp Supergroup (2.754–2.709 Ga, Gumsley et al. 2020). Their contacts to the Stella intrusion are steeply dipping, suggesting the rocks are confined to fault troughs.

The thickness of overburden is typically ~4 m, ranging from 1 to 11 m, the latter in paleochannels. The depth of weathering varies from a few meters to 45 m (average 25 m).

PGE and V-Ti mineralization

The first observation of sulfide mineralization in the Stella intrusion was made by Kafrarian Metal Holdings in 1975–1978 who detected a Cu-Ni-Zn soil anomaly and drilled ferrogabbro. Platinum-group element mineralization was discovered by Anglo American Prospecting Services during the 1990s, following a soil sampling program. Drilling subsequently delineated several mineralized domains. The project is currently estimated to hold measured and indicated resources totaling 69.91 Mt grading at 1.48 g/t Pt+Pd+Au and inferred mineral resources of 56.68 Mt grading 1.62g/t Pt+Pd+Au (unpublished report by Coffey Mining Consultants 2014).

Initial descriptions of the Stella PGE mineralization have been provided by Andrews (2002) and Maier et al. (2003). Close-spaced assaying by Harmony Gold established that the mineralized interval can be sub-divided into several sub-reefs, based largely on PGE, Cu, and Au content as well as Pt/Pd ratio. The stratigraphically lowermost PGE-enriched horizon contains 0.5–3 ppm PGE. It occurs some 15–45 m below the main mineralized interval and has thus been termed "Pre reef kick." The main mineralized interval has an average thickness of 40–45m (Fig. 3). At its base is the low-grade (LG) reef, hosted by magnetite leucogabbro and minor magnetitite. This reef has slightly higher Pt than Pd values, with an overall grade of about 1 g/t Pt+Pd+Au over widths of 10–20 m. The 10–15-m wide mid-reef is Pd-enriched by a factor of 2–4 times relative to Pt. It usually contains two higher-grade reefs, termed MR1 and MR2 (mid-reef 1 and 2, respectively), characterized by elevated magnetite content and grades reaching 4 ppm (average 2.5 ppm) over 1–3 m. Next comes a ~5–10 m, predominantly non-magnetic anorthositic interval with grades of < 0.5 g/t Pt+Pd+Au. The main reef has a width of up to 20 m, with average grade of 1.9 ppm Pt+Pd+Au over 14 m. There are two high-grade zones, the 2.3-m lower main (LM) reef at the base (avg 3.5 g/t Pt+Pd+Au), and the 5–8 m wide, magnetite-rich, upper main (UM) reef at the top (4.4 g/t Pt+Pd+Au). Gold and Cu sharply increase in the top few meters of UM and extend into the hanging wall rocks which consist of magnetite gabbro, magnetite anorthosite, and magnetitite. Relatively low levels of Pt (< 0.3 ppm) and traces of Au persist for ~10 m, whereas elevated Cu continues for ~30 m, to a horizon termed "Pseudoreef," consisting of magnetitite with chalcopyrite but no PGE or Au.

Weathering has resulted in leaching of Pd from the rocks close to surface. Estimated losses within 10 m of surface are 25% Pd and within 30 m 15% Pd. Similar weathering leaching has been reported from the Stillwater Complex (Fuchs and Rose 1974), the Bushveld Complex (Hey 1999; Junge et al. 2019), and the Great Dyke (Oberthür et al. 2013).

Andrews (2002) provided an overview of the platinum group mineral (PGM) variation across the reef interval. He listed kotulskite, moncheite, sperrylite, arsenopalladinite, ferroplatinum, and rare gold and electrum, yet PGE-sulfides are absent. No information on the total number of PGM grains was provided. Most PGM are hosted by silicates, whereas sulfides and magnetite contain few PGM. In some samples, the PGM (particularly sperrylite) may replace silicates and form encrustations (or "atoll structures") around Cu sulfides, up to 35 µm in diameter. There is some variation in the composition of PGM between reefs: LG contains mainly merenskyite and sperrylite, the mid-reef has mainly merenskyite and stibiopalladinite, whereas the main reef has mainly stibiopalladinite and sperrylite. The weathered main reef has abundant PGE alloys and gold, analogous to weathered reefs elsewhere.

The oxides in the oxide layers consist predominantly of titanomagnetite (~85%), with much of the remainder being ilmenite. In addition, some rutile, leucoxene, and hematite are present close to faults. Grades of magnetic fractions of the main reef are 1.14% V_2O_5, 4.83% TiO_2, 81.1% Fe_2O_3 (crater deposit) and 0.93% V_2O_5, 5.59% TiO_2, and 80.7% Fe_2O_3 (Orion deposit) (Andrews 2002). Mid-reef grades (at Orion) are 1.06% V_2O_5, 4.07% TiO_2, 74.2% Fe_2O_3, whereas LR grades at Orion are 0.41 % V_2O_5, 2.36 % TiO_2, 51.3 % Fe_2O_3. Andrews (2002) reported the results of microprobe studies across the drilled interval of the intrusion indicating that magnetite contains an average of 1.3 wt.% V_2O_5, 0.43 wt.% TiO_2, and 0.1 wt.% Cr_2O_3. Vanadium grade drops to 0.9–0.95% V_2O_5 near carbonate alteration but is otherwise relatively constant.

Analytical methods

All whole-rock analyses were performed at LabMaTer, Universitée du Québec à Chicoutimi (UQAC). Tellurium, As, Bi, Sb, and Se were determined on 0.4 g of sample using hydride generation-atomic fluorescence spectrometry (HG-AFS) following Mansur et al. (2020). This method has the advantage of low detection limits in the 3 to 10 ppb range allowing greater precision than standard analytical methods. More details on the method and results for certified reference materials determined in the same batch as the Stella samples are reported in ESM 2b. In addition, a wide range of major and trace elements were determined using laser ablation-inductively coupled plasma-mass spectrometry (LA-ICP-MS) on fused Li-tetraborate disks containing 0.5 g of sample. Details of the method and results for reference materials GeoPt-19, GeoPt-36 (both gabbros), LK-NIP (diabase), and BC28 (massive magnetite) are reported in ESM 2c,d. Analysis of Na, Cs, and Sm by LA-ICP-MS has a markedly higher detection limit than INAA and thus the INAA results from Maier et al. (2003) are used (EMS 2c).

We characterized samples using transmitted and reflected microscopy as well as scanning electron microscopy (SEM). High-resolution element maps were generated using a Carl Zeiss Sigma HD Analytical Field Emission SEM equipped with two Oxford Instruments 150 mm^2 energy dispersive spectrometers (EDS) at Cardiff University. The maps were produced using an accelerating voltage of 20 kV, a 120-µm final aperture in high current mode, a nominal beam current of 8.5 nA, and a working distance of 8.9 mm. For entire sections, a step size of 15–20 µm and a pixel dwell time of 10 ms was used. The acquired maps were processed and exported in AZtec 5.0 software. For the detection of discrete precious metal grains, feature maps were produced, which identifies grains of a user-defined contrast during the automated acquisition of back-scattered electron images. Each identified platinum-group mineral (PGM) was imaged, analyzed by EDS, and morphologically characterized in ImageJ™ software to better constrain their physical and chemical properties.

Results

Drill core observations

Sixty samples from drill core W955D were collected for study. Of these, 26 were analyzed for whole-rock geochemistry. Images of these drill core samples are presented in ESM 1c. The key observations are as follows: (i) due to the greenschist metamorphism identification of the original silicate mineralogy is difficult. However, pseudomorphs of plagioclase can be recognized by their distinctive tabular crystal shapes. Based on geochemistry, the proportion of pyroxene rarely exceeds ~10 modal %. (ii) The rocks are mostly coarse grained, with plagioclase in, for example, samples S11 and S22–25 typically having grain sizes of ~1 cm. Sample S1 is relatively unaltered, showing both mafic minerals (likely hornblende) and plagioclase. (iii) Plagioclase is typically euhedral or subhedral, and, in many cases, defines a well-defined foliation sub-parallel to banding (ESM 1c, d). (iv) Some samples contain pyroxene oikocrysts (S15) and resemble mottled anorthosite. (v) Oxides typically have interstitial habit, possibly resulting from grain boundary adjustment at the sub-solidus stage (Duchesne 1999).

Transmitted and reflected microscopy

The Stella rocks are pervasively altered to a greenschist metamorphic assemblage of clinozoisite, epidote, carbonate, actinolite, and chlorite. This caused near complete replacement of all silicates and partial replacement of magnetite by chlorite, carbonate, and leucoxene and of ilmenite by rutile and sphene. Alteration is particularly pronounced along faults where secondary hematite, rutile, and sphene may occur. As a result of the alteration, no compositional data are available for the primary magmatic minerals. CIPW norms (assuming $Fe^{3+}/Fe^{2+} = 0.3$) of magnetite-poor samples indicate that original plagioclase had anorthite contents of ~55 to 62 (with the exception of sample S1 which appears to have lost some Na), and mafic silicates have Mg# ~0.16 to 0.33.

Small amounts of sulfides occur throughout, but apart from uppermost 25m of the studied sequence where up to ~1% sulfides may occur, their concentration is mostly so low (< 500 ppm S in whole rocks) that they are not readily visible megascopically. The sulfides consist largely of chalcopyrite and pyrite (Fig. 4). Rare phases include pentlandite, millerite, galena, sphalerite, cassiterite, and linnaeite. Most grains are less than 25 µm in size, but a few grains measure up to 500 µm. Chalcopyrite forms anhedral grains that are unaltered, i.e., have no rims of magnetite or bornite. Pyrite mostly forms highly irregular, often vermicular grains that have a porous appearance. The sulfides mostly occur along grain boundaries or cleavage planes of metamorphic silicate minerals that, in most cases, have completely replaced subhedral or euhedral plagioclase crystals.

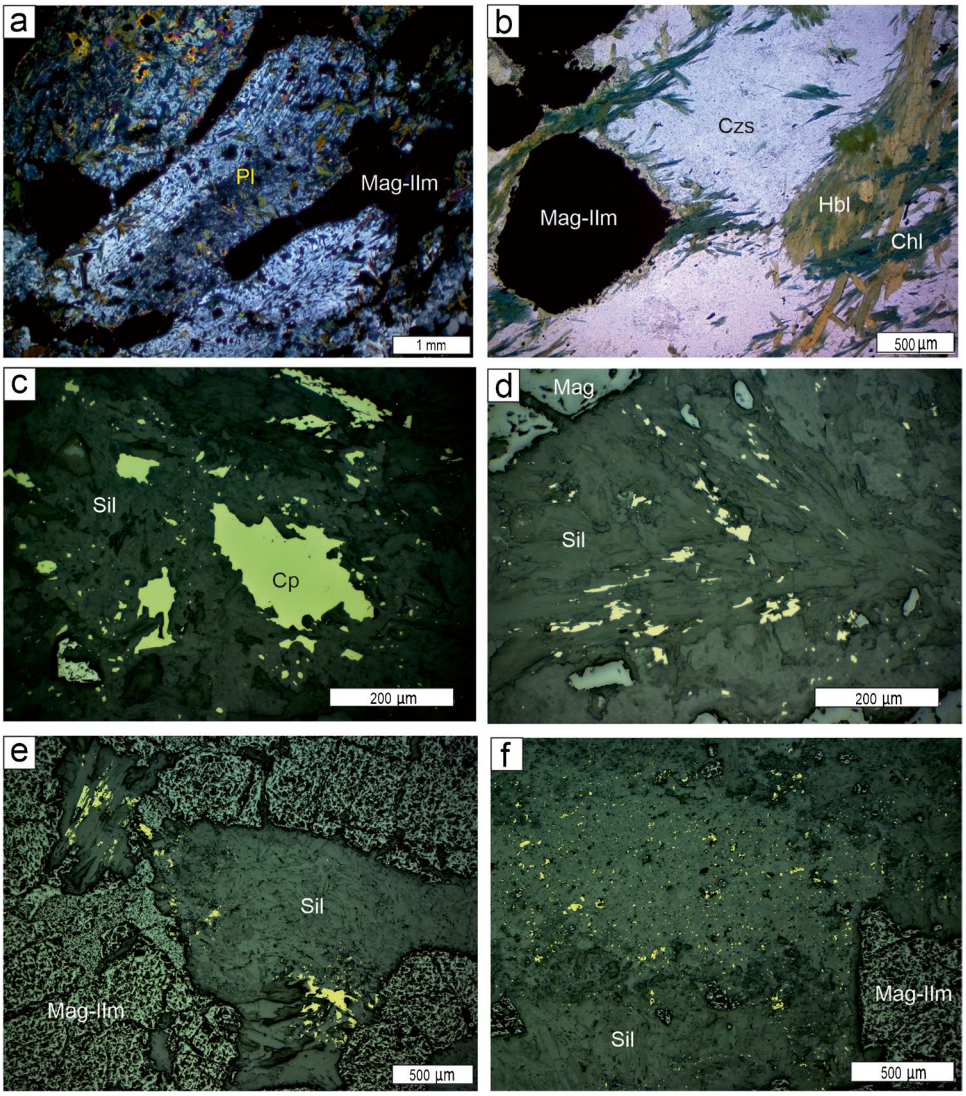

Fig. 4 Petrography of Stella rocks. **a** Pervasive replacement of plagioclase by secondary silicates, including clinozoisite and epidote (center of grain in upper left), as well as disseminated grains of chlorite and hornblende in remaining plagioclase grains. Sample S 2, crossed polars. **b** Metamorphic alteration assemblage affecting plagioclase, sample S2, crossed polars. Czs: clinozoisite; Cl: chlorite; Hbl: hornblende. **c** Anhedral grains of chalcopyrite, lacking alteration rims. Plane polarized reflected light, sample S19. **d** Chalcopyrite filling cleavage planes in actinolite, sample S 19. **e** Chalcopyrite occurring only within silicate minerals, sample S 23. **f** Finely disseminated chalcopyrite in metamorphic silicates, sample S23

Scanning electron microscopy

In order to study the economically important main reef, compositional maps were produced for sample S19 (201.3 m) and its platinum-group mineral (PGM) assemblage was determined. The Fe-Ti-S map (Fig. 5a) highlights the predominance of magnetite over ilmenite, consistent with whole-rock compositional data. Assuming all TiO_2 is in ilmenite, the most oxide-rich samples consistently give proportions of 14 wt.% ilmenite to 86 wt.% magnetite. The Mg-Ca-K-S map (Fig. 5b) shows that the silicate minerals are Ca-rich, with Mg- and K-rich cores, reflecting replacement of plagioclase by sericite and chlorite. The main vein crossing the center of the slide is relatively Mg rich, likely consisting of chlorite and serpentine. The Mg content of the silicates decreases with distance from the vein, possibly reflecting diffusion of Mg from the vein (ESM 1e). The rock contains only few, very small (~10 µm) grains of likely apatite and zircon. The grain areas are close to the step size used (~10 micron); thus, they were unresolvable in our maps. The maps also highlight the relatively small grain size of the sulfides and their predominant association with silicates, whereas oxides are largely sulfide free (Fig. 5c and d).

The BSE images illustrate the distribution of the sulfides and PGM predominantly within silicates (e.g., Fig. 6a), but in rare cases, PGM are associated with sulfide (Fig. 6b) and oxides (Fig. 6c–e). The images also illustrate that the magnetite grains contain trellis-type ilmenite exsolution lamellae which are typically associated with small grains of spinel (Fig. 6e). Granular ilmenite occurs predominantly along grain boundaries of magnetite and near fractures. The ilmenite grains may be surrounded by halos of pure magnetite lacking ilmenite lamellae. Granular ilmenite occasionally is replaced by rutile and titanomagnetite (Fig. 6f).

In total, 164 PGM were characterized in sample S19 (201.1 m), some of which being composite grains of several minerals.

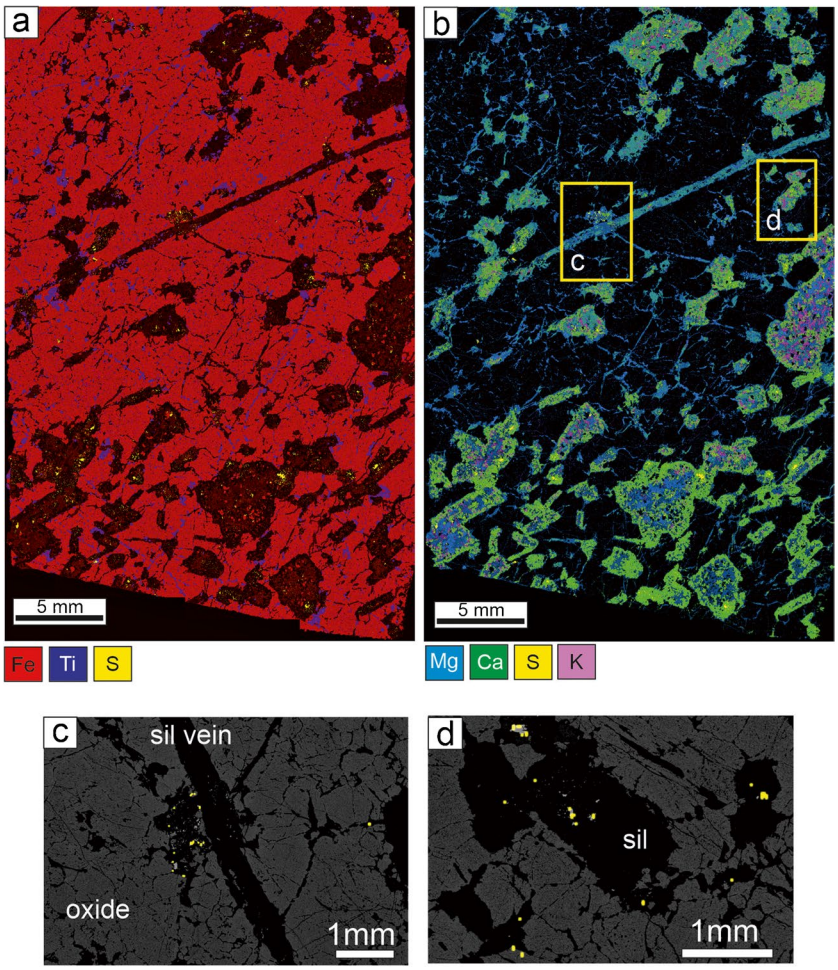

Fig. 5 SEM-EDS element maps of sample S19 (201.1 m). **a**, **b** Note relative scarcity of primary Mg-Ca silicates largely confined to secondary veins and pervasive chloritization of plagioclase. Sulfides are almost exclusively hosted by silicates. Ti is controlled mostly by exsolution phases, plus minor granular ilmenite (and rutile), as well as Ti-rich veins (likely consisting of ilmenite and rutile). **c**, **d** Distribution of PGM, hosted largely in silicates (black), whereas oxides (dark grey) and magnesian veins are largely PGM free

The most abundant mineral is stibiopalladinite (95 grains), followed by sperrylite (68 grains) and kotulskite (22 grains) (ESM 1f, 2f). One grain of Pt-sulfide was found included in magnetite (Fig. 6a). The compositions of the PGMs are relatively homogenous, but some grains of kotulskite have up to 4.6 wt.% Au and 1.3 wt.% Ir, sperrylite has up to 6.5 wt.% Pd and 6.7 wt.% Au, and stibiopalladinite frequently has several wt.% Te and Bi (ESM 2f). The PGM are mostly very small (< 5 µm). On average, sperrylite forms the largest grains, followed by stibiopalladinite and merenskyite. Most of the PGM occur along grain boundaries of metamorphic silicates with a few grains occurring in fractures (7–8% for sperrylite and stibiopalladinite, 1% for merenskyite; Fig. 6). Our work showed a less diverse PGM assemblage than Andrews (2002), likely because we studied just one sample of the main reef, whereas Andrews (2002) studied 7 samples from the main, mid and low-grade reefs.

Lithophile geochemistry

Major oxides

Based on petrography, most Stella samples appear to be mixtures of Fe-Ti oxides and silicates with negligible sulfides or carbonates. Therefore, plots of SiO_2 vs. the other elements give an idea of the composition of the oxide component (Fig. 7). Based on the *y*-axis intercept on a plot of SiO_2 vs. Fe_2O_3 (Fig. 7a), when no silicates are present the Fe oxide component expressed as Fe_2O_3 is 87 wt.%. Plots of SiO_2 versus TiO_2, MgO, and Al_2O_3 give *y*-axis intercepts of 6.6% TiO_2, 2.8% MgO, and 2.7% Al_2O_3 as the concentrations for the oxide component (Fig.7b–d). We can compare these compositions to those calculated by MELTS (see ESM 2g-k) using the composition of a typical

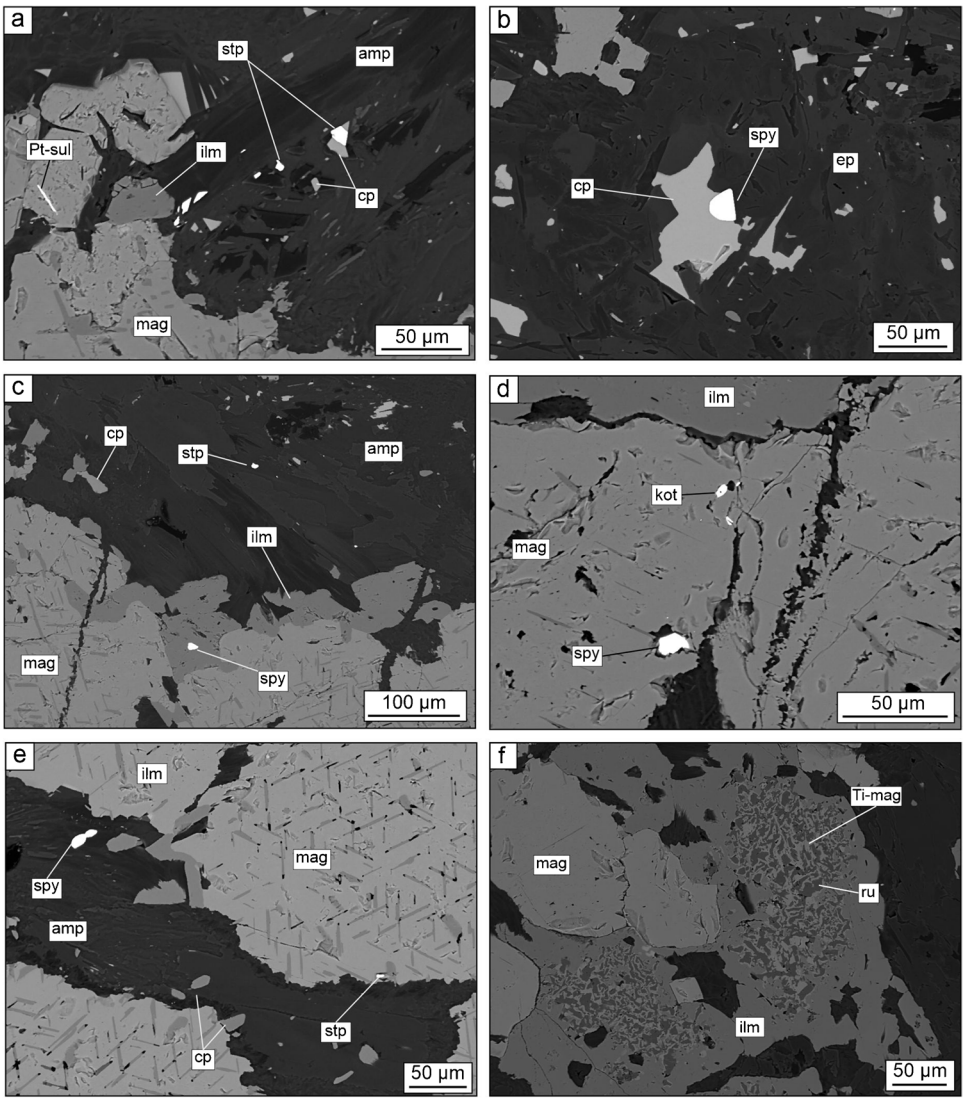

Fig. 6 PGM in sample S19 (201.1 m) of the Stella intrusion. **a** Stibiopalladinite (stp) and chalcopyrite (cp) in silicates interstitial to oxides consisting of magnetite and granular ilmenite. Also note needle-shaped PGM at left, likely representing a Pt-sulfide. **b** Large grain of sperrylite included in anhedral chalcopyrite. **c** Stibiopalladinite within gangue and sperrylite within ilmenite. **d** Kotulskite and sperrylite included within magnetite. **e** Sperrylite (spy) within gangue and stibiopalladinite at margin of magnetite. Note trellis-type ilmenite lamellae as well as abundant small grains of pleonaste. **f** Magnetite and granular ilmenite, the latter breaking down to rutile + titanomagnetite

Archean tholeiite as the magma composition. Fractional crystallization simulations of tholeiite from the Obatogamau Formation, Québec (Boucher et al. 2021), considered to be parental to the magnetite-rich Lac Doré layered intrusion, indicate similar spinel compositions to those estimated at Stella after 75% crystallization. Note that the TiO_2 values are comparable to that of magnetite from the central portion (sub-zone C) of the upper zone of the Bushveld Complex (Klemm et al. 1985) and to magnetite of the Bell River and Lac Doré intrusions, Québec (Polivchuk 2018; Mokchah and Mathieu 2022).

The binary variation plots and the textures suggest that the main silicate component of the Stella rocks was plagioclase. Using the compositions of plagioclase calculated by MELTS for the Archean tholeiite (after 75% fractionation), one can see on plots of MgO vs. SiO_2 (Fig. 7c), CaO vs. SiO_2 (Fig. 7e), and CaO vs. Al_2O_3 (Fig. 7f) that the rocks plot slightly above the plagioclase Fe oxide tie line. Thus, the rocks contain an additional mineral (or minerals) hosting the extra CaO and MgO. Based on the MELTS simulation of Archean tholeiite, this mineral is likely clinopyroxene. Using the plagioclase, magnetite, and clinopyroxene compositions predicted by MELTS, most of the Stella rocks plot near the plagioclase–clinopyroxene tie line with a ratio of plagioclase to clinopyroxene ~1 : 9. In summary, the major element composition of the whole rocks can be modeled as mixtures of magnetite, plagioclase, and clinopyroxene. The proportion of plagioclase to clinopyroxene is fairly constant at 9 : 1 whereas the magnetite content varies widely from 1 to 90%.

Transition metals

Vanadium, Ni, Co, and Zn all show negative correlations with SiO_2 suggesting that these elements too are mainly controlled by mixtures of Fe-Ti oxides with silicates (see Fig. 7g for V, ESM 2l for Ni, Co, and Zn). The intercepts for

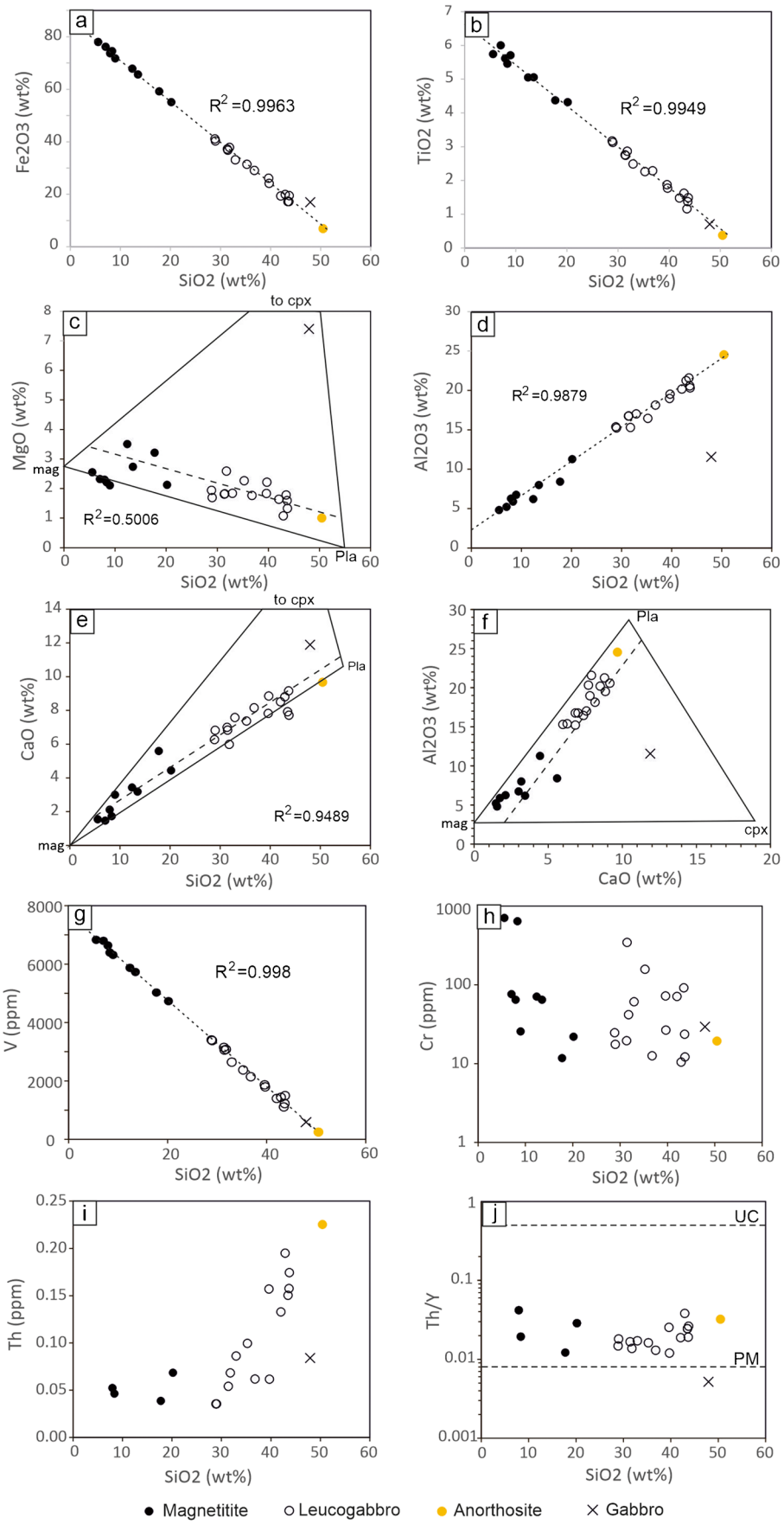

Fig. 7 Binary variation diagrams of Stella rocks. **a** Fe_2O_3 vs. SiO_2, **b** TiO_2 vs. SiO_2, **c** MgO vs. SiO_2, **d** Al_2O_3 vs. SiO_2, **e** CaO vs. SiO_2, **f** Al_2O_3 vs. CaO, **g** V vs. SiO_2, **h** Cr vs. SiO_2, **i** Th vs. SiO_2, and **j** Th/Y vs. SiO_2. Mineral compositions in c, e, and f are from MELTS simulation of Obatogamau Archean tholeiite after 75% fractionation. Trend lines in a, b, d, and g are calculated for data excluding gabbronorite sample. Stippled line in **c**, **e** and **f** indicates proportion of clinopyroxene is 10%. Composition of UC and PM in j are from Rudnick and Fountain (1995) and Sun and McDonough (1989), respectively

these elements at 100% oxide suggest that magnetite contains ~1.2% V_2O_5, ~650 ppm Ni, ~250 ppm Co, and ~250 ppm Zn. The V content is slightly lower than that of the main magnetite layer of the Bushveld Complex (~1.5–2% V_2O_5) which is mined for V, but is similar to magnetitite in the center of the Bushveld upper zone (sub-zone B) and to magnetite at Bell River and Lac Doré (Polivchuk 2018; Mokchah and Mathieu 2022).

Manganese (intercept ~0.24 wt%) and Sc (intercept 20 ppm) show slightly weaker correlations with SiO_2 (ESM 2l) suggesting that these elements are slightly less compatible with magnetite than V, Ni, Co, and Zn. For both elements the gabbronorite at the base of the mineralized interval (sample S1) plots at high levels of Sc and Mn, possibly because these elements are more compatible with clinopyroxene than Fe oxide (Ewart and Griffin 1994; Otamendi et al. 2016).

Chromium does not correlate with SiO_2 or anything else (Fig. 7h). Our data indicate < 100 ppm Cr in most samples, except for the two lowermost magnetitites (S5 and S7) that have ~700 ppm Cr. Interestingly, semi-massive magnetite sample S4, located just 5 m below Cr-rich magnetitite sample S5, has only 11 ppm Cr although V tenors are broadly similar as in S5. This indicates a surprising degree of decoupling of V and Cr contents of magnetite, considering that Cr and V are both strongly compatible into magnetite (D_{Cr} mean 67, range 19–340; D_V mean 26, range 7–130; Dare et al. 2012). The data are not an analytic artefact as INAA analysis (Maier et al. 2003) yielded similar results. Possibly, a more primitive magma intruded at the level of sample S5, or in the Cr-poor samples clinopyroxene crystallized together with magnetite, competing for Cr.

Rare earth elements

All REE are incompatible with magnetite and show negative correlations with Fe_2O_3+TiO_2 and SiO_2 (not shown). Europium is the least incompatible with regard to plagioclase, with a partition coefficient approaching unity (Bédard 2006). On REE multi-element diagrams (ESM 1g), the silicate-rich rocks all have strong positive Eu anomalies reflecting the presence of cumulus plagioclase in these rocks. The patterns are relatively flat, resulting in La/Yb_N ~1.44. Gabbronorite sample S1 has a relatively flat REE pattern with mostly higher REE contents than the other cumulates, suggesting it has a higher melt component than the other samples. The magnetite-rich samples all have relatively low REE contents, with less pronounced positive Eu anomalies, consistent with their low plagioclase content.

HFS and LIL elements

Hafnium, Zr, Nb, and Ta are incompatible with regard to plagioclase and clinopyroxene. They have small but significant D values into Fe oxides (0.13 to 0.25, Dare et al. 2012). Hafnium and Ta are both present at very low levels in all rock types and the concentration of both elements is similar (0.3–0.6 and < 0.03–0.09 ppm, respectively). The slight compatibility of Zr, Hf, Nb, and Ta with regard to magnetite precludes using these immobile elements to estimate trapped liquid component. Samarium is not compatible with any of the crystallizing minerals. Assuming that the magma contained Sm concentrations similar to the Archean tholeiite, and allowing for 75% fractional crystallization, the trapped liquid should contain ~4.5 ppm Sm. The Stella cumulates contain 0.1 to 0.6 ppm Sm which suggests 2 to 13% trapped liquid.

Thorium is incompatible with plagioclase, clinopyroxene, and magnetite and thus should broadly reflect the trapped liquid component of the rocks. All analyzed samples have relatively low Th contents (< 0.25 ppm, Fig. 7i), reflecting their cumulate nature. The plagioclase-rich rocks have the highest Th contents, suggesting either that they contain a higher liquid component than the magnetitites, perhaps due to less efficient compaction, or that they assimilated some crustal material. To assess the possibility of crustal contamination, we have elected to use Th/Y ratios since these elements are both strongly incompatible with respect to plagioclase and Fe-Ti oxides. In addition, Th/Y in the upper crust and the mantle is very different (UC: 0.49, PM: 0.019). Yttrium is slightly compatible into clinopyroxene, but clinopyroxene is a minor component of the Stella rocks. The Stella rocks have Th/Y between 0.01 and 0.05, broadly similar to PM (Fig. 7j). Based on these data, contamination does not appear to be a critical factor in the crystallization of the Stella rocks. This interpretation is consistent with the generally unfractionated nature of multi-element variation diagrams of lithophile incompatible trace elements (ESM 1h), with the exception of positive Sr, Eu, and Ti anomalies representing cumulus plagioclase and magnetite, and elevated concentrations of large ion lithophile elements K, Ba, Cs, and Rb. The latter show erratic correlations with Na, possibly due to variable alteration. Given that the samples have experienced greenschist facies metamorphism these elements will not be considered further.

Chalcophile elements

Copper, Au, Se, Sb, As, Te, Bi, and the PGE are all chalcophile elements under crustal conditions and are thus expected to be controlled by sulfides. Therefore, the correlations between these elements and S will be considered first (Fig. 8).

Copper shows a good positive correlation with S, but there are three distinct populations (Fig. 8a). Most samples containing > 0.5% S have S/Cu ratios of approximately 1.5,

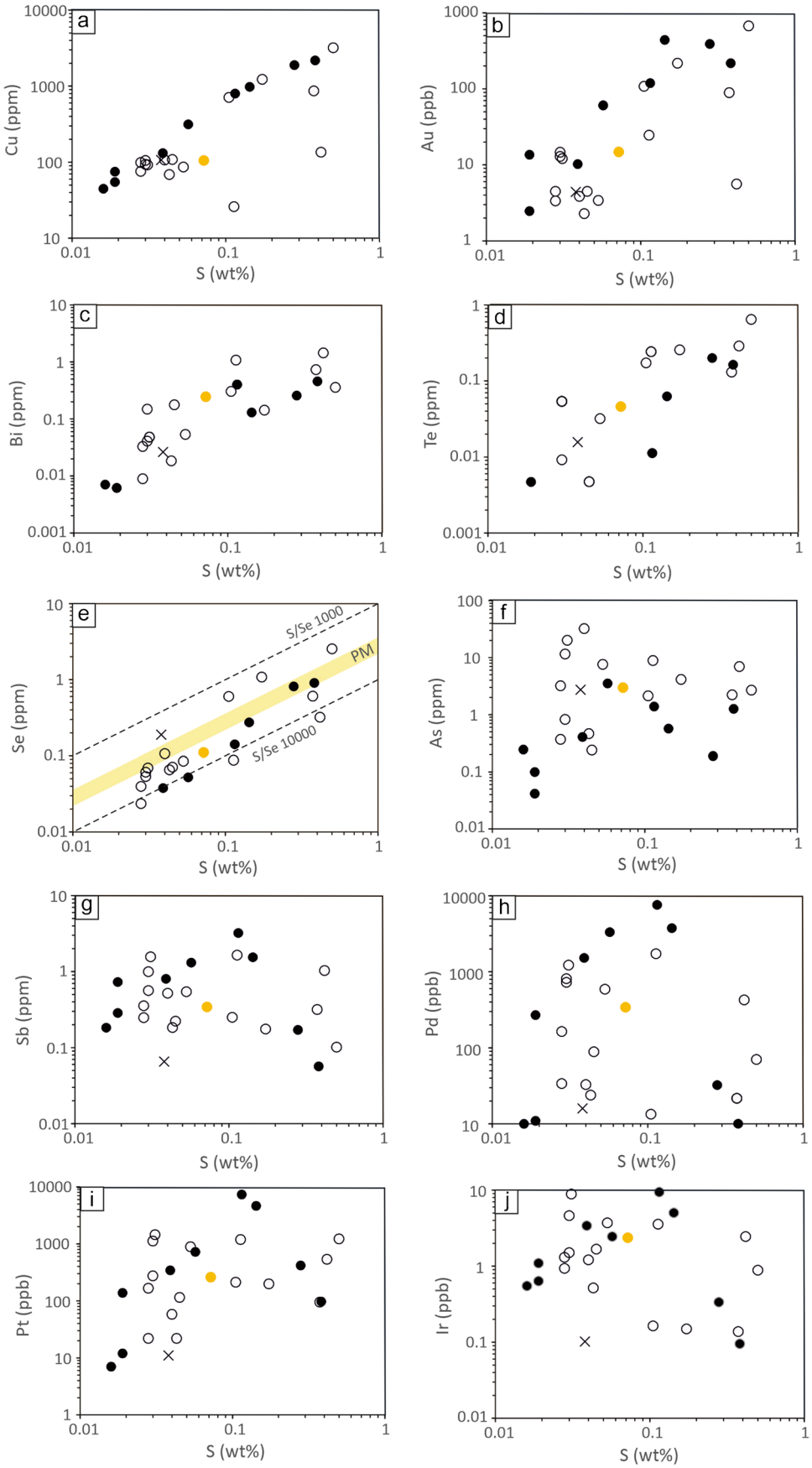

Fig. 8 Binary variation diagrams of chalcophile metals vs sulfur (x = gabbro, orange dot is anorthosite). **a** Cu, **b** Au, **c** Bi, **d** Te, **e** Se, **f** As, **g** Sb, **h** Pd, **i** Pt, and **j** Ir

indicating that the main sulfide phase is probably chalcopyrite (S/Cu~1). As mentioned earlier, Ni appears to have been largely controlled by the oxides. In rocks with > 0.3% S, the ratio of Ni/S is ~0.05 implying the Ni content of the sulfides is ~1.7%; therefore, < 5% of the sulfides are pentlandite, with the remaining sulfide phase probably being Fe-sulfide (pyrite), consistent with petrographic observations. The samples with relatively low S concentrations (< 0.5 %) have S/Cu ratios of ~3; these would then contain ~1/3 chalcopyrite and 2/3 pyrite. Seven samples plot below these trends, possibly indicating S addition or Cu loss. Taken together, the three populations suggest a Cu-rich sulfide, a medium-Cu sulfide, and some low-Cu sulfide.

Gold, Te, Bi, and Se also show positive correlations with S, consistent with their high D values into sulfide melt (Fig. 8b–e) (Barnes 2016), albeit with more scatter than Cu.

Se/S ratios are commonly used to evaluate addition of external S to a magma (Eckstrand et al. 1989; Queffurus and Barnes 2015 and references therein) and are thus of particular interest. For samples with Se contents higher than the detection limit there is a positive correlation between S and Se, but with highly variable S/Se. Most samples have S/Se > 5000, i.e., non-magmatic values normally explained by addition of external S to a magma (Queffurus and Barnes 2015). Five samples have S/Se > 10000, yet most of the samples with high S/Se are relatively S-poor. However, when the bulk S and Se contents of the entire interval are considered the S/Se is 3500, i.e., overlapping with the magmatic range of S/Se (2850-4350; Eckstrand and Hulbert 1987).

Arsenic and Sb do not correlate with S (Fig. 8f and g). There are two main populations, namely, the magnetitites and the magnetite-bearing anorthosites. Both have moderate correlations between As and Sb (not shown), with the former having markedly lower As/Sb ratios.

Correlations between Pt and Pd with S are generally poor, particularly in the samples with > 0.15% S (Fig. 8h and i). Platinum, Pd and Ir show positive correlations with each other (ESM 1i), suggesting that none of the PGE was significantly mobile. The PGE show strong positive correlations with Sb (ESM 1i), but not with As (ESM 1i), suggesting they are mainly controlled by antimonides. For all PGE-enriched samples the ratio of Pd to Sb is 1 to 2 in terms of weight. As the atomic weight of Pd and Sb is broadly similar, the antimonides thus should be predominantly PdSb and Pd_5Sb_3, i.e., approaching the composition of stibiopalladinite, in agreement with the observed PGM assemblage.

In order to further constrain the behaviour of the chalcophile elements during partial melting, crystallization, and crustal contamination, we plotted the compositions of high-S and low-S samples into mantle normalized multi-element plots after Barnes and Mansur (2022) (Fig. 9). Contamination with continental crust results in enrichment in Th, As, Sb, and Bi, as well as negative Nb anomalies, as has been previously shown for the Bushveld Complex (Mansur and Barnes 2020). The Stella rocks, including the magnetite poor samples, lack negative Nb anomalies, suggesting that crustal contamination was insignificant or involved incompatible-trace-element-poor material. The S-rich rocks have broadly similar levels of Te, As, Bi, Sb, Se and PGE, but many of the S-poor rocks are enriched only in As, Sb and Bi. This confirms that there is a decoupling between the PGE and most other chalcophile elements (Fig. 8, ESM 1i).

Of particular interest are the patterns of sample S1 (Fig. 9). The sample is barren in terms of PGE as well as Se and Te (ESM 2e) but is enriched in crust-derived As-Sb-Bi, i.e., PGE and crust-derived chalcophile elements are decoupled. This suggests that As, Sb, and Bi were introduced to the rocks by crust-derived metamorphic fluids or assimilation of crustal rocks.

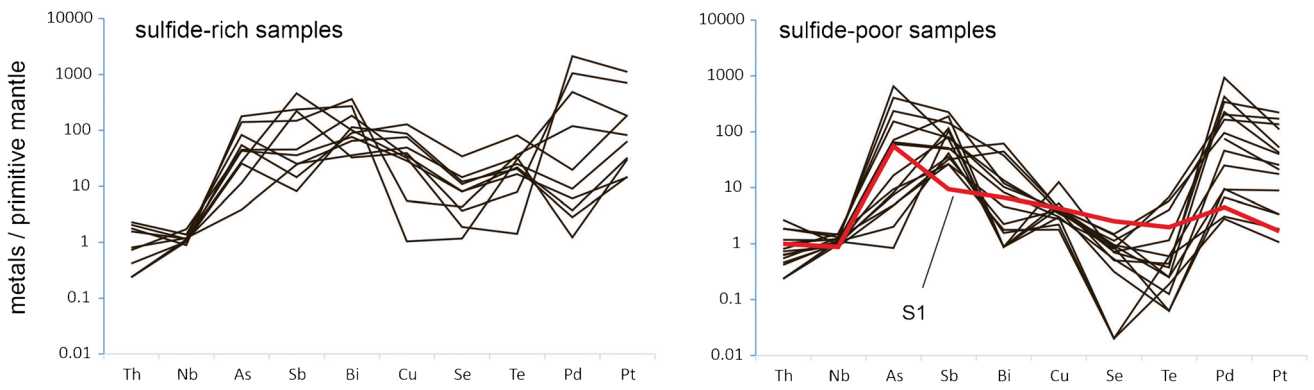

Fig. 9 Multi-element variation diagram of TABS as well as Th and selected PGE, normalized to primitive mantle (normalization factors from Lyubetskaya and Korenaga 2007)

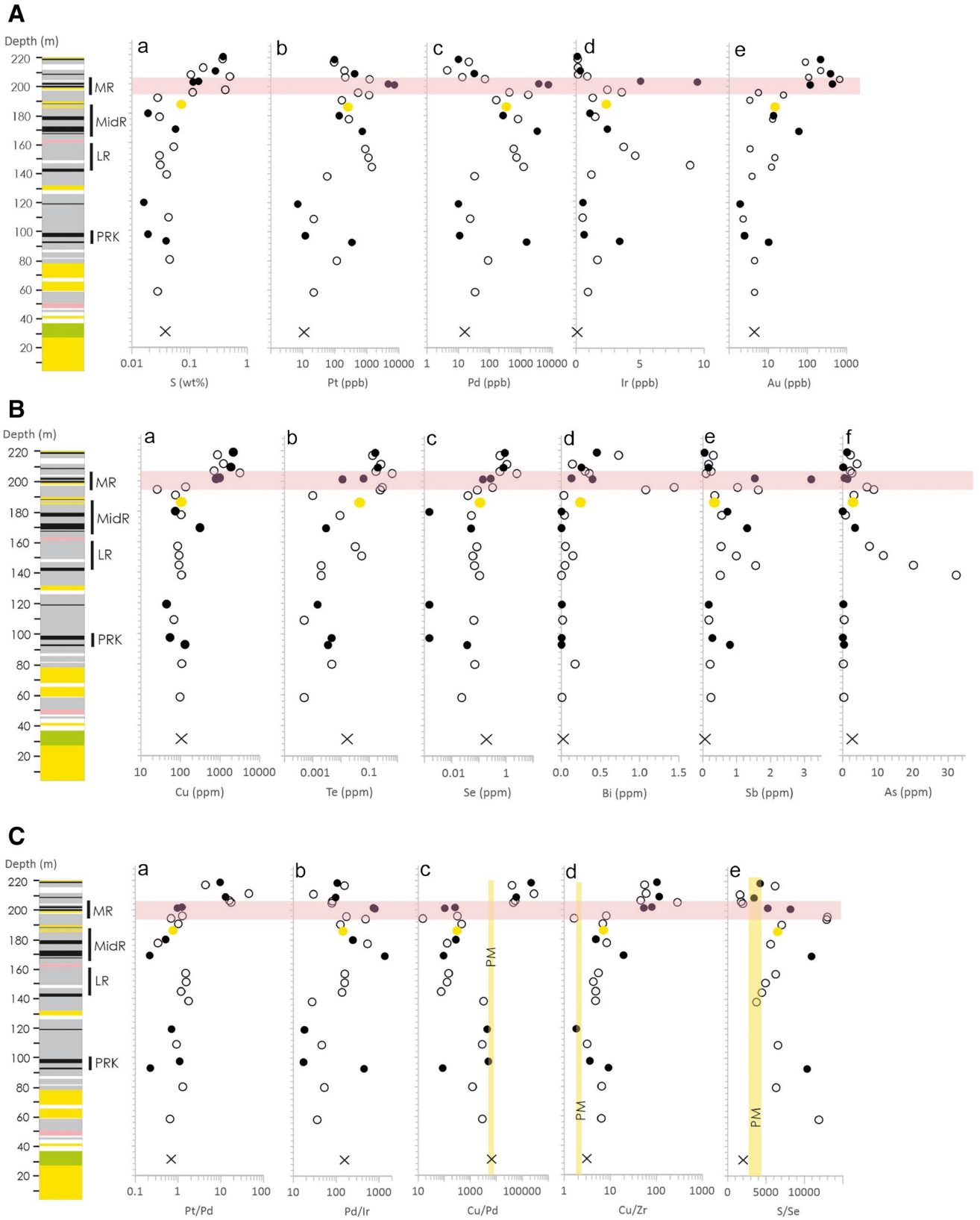

Fig. 10 **a**–**c** Diagrams showing concentrations of lithophile and chalcophile elements and element ratios plotted vs. stratigraphic height in drill core W955D. **a** Sulfur and noble metals, **b** copper and TABS, and **c** chalcophile element ratios. Numbers next to logs denote depth of drill core (in meters) which broadly represents stratigraphic height of intrusion

Vertical compositional variation

The distributions of selected lithophile elements and element ratios, as well as S, Cu, TABS and the noble metals in the analyzed drill core are plotted vs height in Fig. 10 and ESM 1j. Several observations may be highlighted:

(i) Most major element oxides, including TiO_2 (and Fe_2O_3, not shown) as well as trace elements V (and Zr, not shown) display no clear trend with height (ESM 1j). Al_2O_3, reflecting plagioclase mode, increases with height, whereas Cr decreases with height (ESM 1j). Th/Y, potentially a proxy for contamination, is slightly enriched in the reef interval relative to the footwall rocks.
(ii) Sulfur shows relatively low concentrations (200–700 ppm) up to a stratigraphic height of ~195 m, above which there is a sharp increase to 1100–5000 ppm (Fig. 10a). A similar pattern is seen for Cu, Te, Se, Bi, and Au (Fig. 10b), elements that show positive correlations with S in binary variation plots (Fig. 8).
(iii) The concentrations of the PGE (Fig. 10a) and Sb (Fig. 10b) also increase with height, albeit showing considerable scatter and several peaks.
(iv) Arsenic behaves differently from the other chalcophile metals, showing the highest concentrations in magnetite anorthosite in the central portion of the interval (Fig. 10b).
(v) The thickness of the main mineralized interval, containing > 1000 ppb PGE + Au, amounts to some 70 m (Fig. 10a). Particularly elevated concentrations are found at a stratigraphic height of ~100 m (the so-called "pre-reef kick"), 145–160m (the "low-grade reef"), 160–185 m (the "mid-reef"), and 190–202 m (the "main reef").
(vi) Whereas the highest PGE grades are found in three magnetite layers, some magnetite layers are virtually barren and some silicate-rich samples are PGE enriched such that magnetite and PGE concentrations are decoupled (Fig. 10a).
(vii) Peak values of different chalcophile metals occur at different stratigraphic levels (Fig. 10a and b); Rh peaks at 93 m and 145 m above the base of the intrusion, Ir at 145 m and 201 m, Pt+Pd at 201–202 m, Au at 202–205 m and Cu at 205–219 m. Te and Se peak at the same stratigraphic level as Cu, but As peaks at 140 m, Bi at 195 m, and Sb at 200 m. This pattern of stratigraphic separation of peak concentrations has been termed "offset" mineralization in the Munni Munni intrusion (Barnes et al. 1992) and the Great Dyke (Wilson et al. 2000; Oberthür and Cabri 2002).
(viii) Chalcophile element ratios Cu/Pd and Pt/Pd show sharp increases above the main reef, analogous to other PGE reefs, such as the Bushveld Complex (Fig. 10c). Pd/Ir of the mineralised rocks plots mostly between 100 and 800, consistent with the relatively evolved nature of the Stella rocks.
(ix) Cu/Zr in the studied interval is generally above the level of the primitive mantle (Fig. 10c) reflecting the presence of sulfides in all rocks. Cu/Zr sharply increases above the main reef. This is surprising as one would normally expect that the formation of a PGE reef depletes Cu relative to Zr.
(x) S/Se is mostly above the range of the primitive mantle (Fig. 10c), except for the S- and Se-rich uppermost samples with overlap with the S/Se range of the primitive mantle.

Discussion

Comparison of Stella to other PGE mineralized layered intrusions

The major PGE reef-type deposits are located in the lower to central portions of layered intrusions such as the Bushveld Complex of South Africa, the Stillwater intrusion of Montana/USA and the Great Dyke of Zimbabwe. Most subeconomic PGE reefs occur in similar settings (Smith and Maier 2021). However, in a number of layered intrusions, elevated PGE grades have been found in the relatively evolved, magnetite-rich upper portions of the intrusions. Possibly the first such occurrence was reported by von Gruenewaldt (1976), describing PGE rich sulfides below the main magnetite layer (MML) of the Bushveld Complex. Subsequently reported examples include the 2435 Ma Koitelainen intrusion of northern Finland (Mutanen 1989), the 55 Ma Skaergaard intrusion of Greenland (Bird et al. 1991), the Birch Lake deposit of the 1107 Ma Duluth Complex (Hauck et al. 1997), the 992 Ma Rincon del Tigre intrusion of Bolivia (Prendergast 1998), the 1096 Ma Sonju Lake intrusion within the Duluth Complex of Minnesota (Miller Jr. 1999), the 1108 Ma Coldwell Complex of Ontario (Barrie et al. 2002), the ~2640 Ga Rio Jacare Complex in Brazil (Sa et al. 2005), the 3033 Ma Stella layered intrusion (Maier et al. 2003), the Jameson intrusion of Western Australia (Maier et al. 2015, Karykowski et al. 2017), and the Nuasahi intrusion of India (Prichard et al. 2018). These PGE-enriched horizons share a number of common features. They have widths of several 10 s of meters (~60 m at Stella, 42–95 m at Rincon del Tigre, 60 m at Skaergaard, 75 m at Koitelainen, at least 25 m at Sonju Lake, up to 80 m in the Coldwell Complex, ~110 m in the Rio Jacare Complex, and ~20 m at Birch Lake). Most show a distinct "offset" pattern, with PGE peaking below Cu and Au. However, apart from the Stella reefs, only the

Skaergaard reefs (~5.5 ppm Pt+Pd in a 1-m-thick layer) and Birch Lake (7–9 ppm Pt+Pd over ~5 m) approach economic grade. In contrast, at Rincon del Tigre, peak values are 1.8 ppm Pd over 1 m. At Koitelainen, peak values reach ~1–1.5 ppm over ~4 m. At Rio Jacare, peak values are 1.5 ppm over 1 m. At Skipper Lake in the Coldwell Complex, peak values are 1.6 ppm PGE over 3.4 m. At Jameson, 1-2 ppm PGE occur over 1-2m.

Metamorphism

The Stella rocks contain a typical middle greenschist facies metamorphic assemblage. Based on the strong correlations between SiO_2, Al_2O_3, Fe_2O_3, and most lithophile elements, we conclude that the effect of metamorphism has not changed the concentrations of these elements. Exceptions are Cs, Rb, and K which appear to be enriched relative to less mobile elements, probably when plagioclase was replaced by sericite, and Na and Ba which appear to have been partly lost, especially from the magnetite rich rocks. There is no correlation between K_2O or SiO_2 and any of the chalcophile elements, so the metamorphic alteration is likely not the reason for the decoupling of PGE, Sb and As with S and Cu.

State of differentiation and magmatic lineage of the Stella layered intrusion

Iron–titanium oxide layers are typically found in the upper portions of layered intrusions which implies that Fe-Ti oxides crystallize only after the magma has undergone considerable fractionation. In some layered intrusions, oxides may occur near the base (e.g., Panzihua, Hongge, and Baima), and in these cases, it has been proposed that the intruding magma may be relatively evolved and Fe-enriched (Song et al. 2013).

The crystallization of Fe oxides has been experimentally investigated by Toplis and Carol (1995) using a fine-grained dyke from the base of the Skaergaard intrusion as a starting composition (~6.5 wt.% MgO). The exact timing of the appearance of Fe oxides depends on the oxygen fugacity. Assuming fO_2 at FMQ, some 60% crystal fractionation of olivine, plagioclase, and clinopyroxene is required before Fe oxide crystallizes.

The crystallization history of the Stella intrusion has been modeled using rhyolite MELTS simulations (Smith and Asimow 2005) of fractional crystallization of Archean tholeiite (6.34 wt.% MgO) from the Obatogamau Formation (Boucher et al. 2021). The simulations indicate that ~50% fractionation is needed to bring Fe oxide on the liquidus of the tholeiite (Fig. 11), but to crystallize minerals of the composition suggested by the Stella CIPW norms such as the An content of plagioclase of ~55, the tholeiite likely underwent ~75% fractionation.

The relatively unfractionated incompatible trace element patterns (ESM 1h) and essentially flat chondrite-normalized REE (ESM 1g), as well as the mantle-like Th/Y values (Fig. 7j) suggest that the Stella rocks did not undergo significant crustal contamination.

Origin of layering

The major element plots of the Stella rocks suggest two end-member compositions. The first end-member contains up to 90% magnetite as well as minor clinopyroxene and plagioclase (in the ratio of 1 : 9). The second end-member comprises predominantly silicate minerals, with ~85% plagioclase, ~9% clinopyroxene, and ~6% Fe oxide. This suggests that the studied interval consists essentially of interlayered magnetite-bearing anorthosite and leucogabbros. Such rocks represent non-cotectic assemblages which could be explained by a range of petrogenetic models.

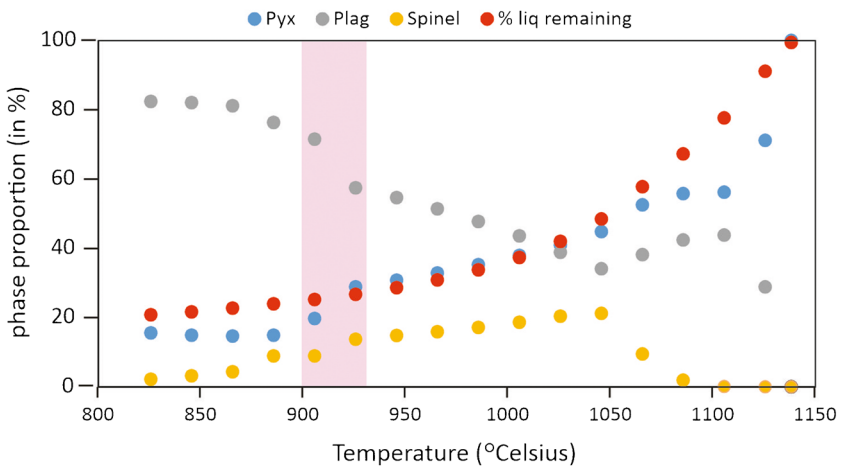

Fig. 11 MELTS simulation of crystallization of Archean tholeiite (sample 152A1, Obatogamau Formation, Boucher et al. 2021). Pink field denotes likely crystallization interval of analyzed Stella rocks. See text for further explanation, and ESM 2g-k for the outputs of the simulation

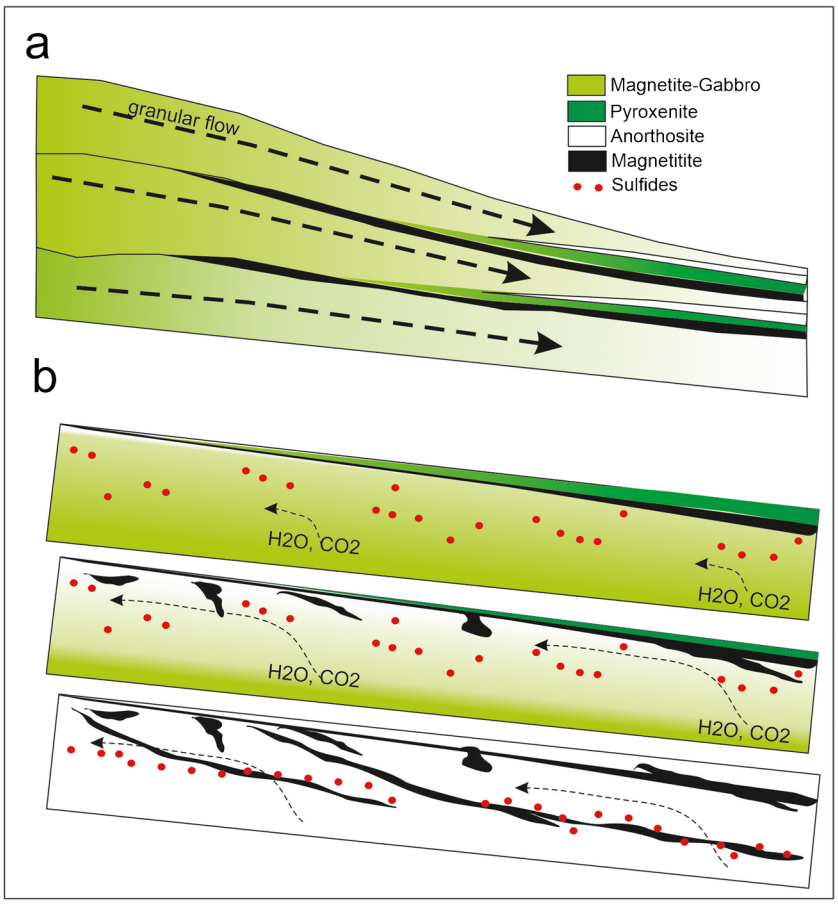

Fig. 12 Sketch model of proposed formation of Stella layering. **a** Granular flow of gabbroic crystal mushes resulting in distinct pyroxene-, oxide-, and plagioclase-rich layers. Arrows indicate flow direction. **b** Reactive flow of volatiles trapped in sulfide-bearing magnetite gabbro beneath magnetite layers causes dissolution of pyroxene, resulting in percolation of magnetite into volatilerich, sulfide-bearing anorthositic mush, forming lenses and layers of oxide-rich rocks

(i) Accumulation of a broadly cotectic plagioclase–clinopyroxene–magnetite crystal mush (in proportions of ~70 : 20 : 10, Fig. 11), followed by granular flow causing phase sorting and sieving. Analog experiments of Forien et al. (2015) have simulated granular flow of plagioclase–pyroxene–oxide slurries resulting in distinct layers of oxide, pyroxene, and plagioclase. This model is schematically shown in Fig. 12a. Granular flow would potentially provide an explanation for the pronounced lateral thickness variation of layers reported by Andrews (2002) and the preferred orientation of plagioclase grains (ESM 1c,d). However, none of the analog experiments generated interlayered oxide-only and plagioclase-only mushes without interleaved pyroxenite, as observed at Stella.

(ii) Plagioclase flotation. This model was initially suggested by Bowen (1917) for massif-type anorthosites, by Vermaak (1976) for Bushveld anorthosites and by Higgins (2005) and Namur et al. (2011) for the thick anorthosite under the roof of the Sept-Iles intrusion, Québec. However, plagioclase flotation cannot readily explain the interlayering of anorthosite with relatively dense magnetite layers.

(iii) Intrusion of plagioclase supersaturated magma (Latypov et al. 2020) into magnetitite. However, the model liquids proposed by Latypov et al. (2020) have no match in nature.

(iv) Reactive porous flow. Meurer et al. (1997) have argued that relatively cool, silica and alkali undersaturated volatiles ascending through a cumulate pile can trigger dissolution of pyroxene and sodic plagioclase while stabilizing calcic plagioclase. Maier et al. (2021) used this model to explain Bushveld anorthosite layers. In the case of Stella, one could argue that volatiles were trapped in sulfide-bearing magnetite gabbro beneath a relatively compacted layer of magnetitite (Fig. 12b). This could have triggered transformation of the gabbro to leucogabbro and anorthosite, while facilitating sinking of dense magnetite crystals into the volatile-rich silicate mush. If the latter underwent granular flow, layers of magnetite-anorthosite as well as magnetitite of laterally highly variable thickness could have formed, both being locally enriched in PGE. The model would also offer an explanation for the widely observed association of oxide layers with anorthosites in layered intrusions (e.g., Cawthorn and Ashwal 2009).

Origin of the Stella PGE mineralization

The formation of PGE reefs remains debated, likely comprising both syn-magmatic and late-magmatic processes (Naldrett

2004; Boudreau and McCallum 1992; Smith et al. 2021; Mansur et al. 2021). In the following section, we aim to place constraints on the relative importance of these processes.

PGE reef formation by syn-magmatic processes

Sulfur is incompatible into silicate minerals. As a result, crystallization leads to an increase in S content of the magma, ultimately triggering sulfide melt saturation. For example, Barnes et al. (2009) have shown that Bushveld B1 magma reaches sulfide melt saturation after ~15% fractionation, broadly consistent with estimates of Ripley and Li (2013) for siliceous high-Mg basalt and picrite (15–25%), explaining the occurrence of most high-grade PGE reefs in the lower portions of layered intrusions. However, at Stella, high-grade PGE reefs occur in the upper portion of the intrusion. This could suggest that initial sulfide melt saturation occurred relatively late, possibly due to Fe enrichment of the crystallizing magma (Li and Naldrett 1993; Scoates and Mitchell 2000; Ripley and Li 2013). An example is Kiglapait where sulfide melt saturation occurred at 91% crystallized (Morse 1981). Von Gruenewaldt (1976) proposed that sulfide saturation in evolved magmas may be triggered by magnetite crystallization resulting in a sharp drop in Fe contents of the magma, consistent with the observation that many of the PGE reefs in the upper portions of LI occur in magnetite-rich intervals. Furthermore, fractional crystallization simulations of Archean tholeiite indicate that sulfide melt saturation is attained at ~65% fractional crystallization, just after spinel has appeared on the liquidus (Fig. 11, ESM 2g-k).

Mobilization of PGE and TABS by high-T fluids

The mineralized interval at Stella shows a number of features that could suggest an important role for fluids in petrogenesis. For example, the silicate minerals are metamorphosed. The S/Se ratios are highly erratic and, in much of the interval, significantly higher than mantle. Pyrite is abundant, locally forming the predominant sulfide. There is a relatively weak correlation between the PGE and S whereas the PGE correlate with Sb, suggesting control of PGE by antimonides. Arsenic and Sb are locally enriched, despite relatively low D values with respect to sulfide melt.

We consider two main models by which fluids could have controlled or modified the PGE mineralization: firstly, the PGE reefs could be of largely secondary origin caused by introduction of PGE via late magmatic or hydrothermal fluids originating in weakly mineralized floor cumulates (Schiffries 1982; Ballhaus and Stumpfl 1986; Boudreau and McCallum 1992). However, large-scale mobility of Pt and Pd in fluids at Stella is not consistent with the observed positive correlation between Pt and Pd with IPGE (ESM 1i), the latter normally being considered immobile (Holwell et al. 2017), although experimental data are lacking. Secondly, the Stella reefs could be of largely primary magmatic origin but were upgraded due to local mobility of S and chalcophile elements in deuteric fluids, as proposed by Anderson et al. (1998), Sluzhenikin et al. (2020), Sa et al. (2005), Dijon and Barnes (2012) and Li and Boudreau (2017) for Skaergaard, Noril'sk, Rio Jacare, and Lac des Iles, respectively. Mansur et al. (2021) argued that during deuteric or metamorphic alteration of magmatic sulfides in the Luanga intrusion, Brazil, Se, Te, Bi, and Pd were lost together with S, whereas As and Sb combined with PGE to form PGM. Thus, As and Sb would have acted as fixing agents for PGE (especially Pt), along the models of Mountain and Wood (1988) who showed that the effect of As, Se, and Te is to decrease the mobility of Pt and Pd, and of Wood and Cabri (2002) who suggested that free arsenide or telluride should trigger the formation of insoluble PGE phases. Some aspects of this model can be applied to Stella. The first stage in reef formation involved sulfide segregation in response to advanced fractionation, resulting in a ~100-m-thick PGE-enriched gabbro with relatively high PPGE/IPGE ratios and enrichment in Au, Cu, and TABS (Fig. 12b). Late magmatic fluids then redistributed S, Cu, Te, Bi, and Se from the lower to the upper portion of the reef interval. The occurrence of S/Se values above primitive mantle levels in many of the most S and Cu depleted rocks in the lower part of the PGE mineralized interval suggests that there were several pulses of fluid flux, with early removal of S followed by late-stage reprecipitation of S. In contrast, the PGE and As were relatively immobile, delineating the original position of the sulfides. Mountain and Wood (1988) do not provide data for Sb, but if we argue that Pt and As are not moving significantly then by analogy PdSb has to be immobile at Stella since it is concentrated in the same rocks.

We acknowledge that there are several observations which cannot be explained solely by local-scale mobilization of magmatic Pd, Te, Se, and Cu in late magmatic fluids. For example, Andrews (2002) reported encrustations of sperrylite around Stella BMS suggesting that Pt and As were locally mobile (Sullivan et al. 2022), possibly in domains where the sulfides were completely dissolved (Holwell et al. 2017). Most significantly, As and Sb contents are typically decoupled from PGE and the other TABS, as for example in gabbro sample S1 at the base of the analyzed interval that is barren in PGE and Te-Se, but enriched in As, Sb, and Bi (Fig. 9). This suggests addition of the latter metals from the crust, such as sulfide and As-Bi-rich banded iron formation that was intersected by drill cores at in the Kalahari Goldridge gold deposit of the Kraaipan greenstone belt (Hammond and Moore 2006). Because Stella shows little lithophile element evidence for crustal contamination (ESM 1g,h), As, Sb, and Bi were likely introduced by fluids.

Implications for exploration

Economic PGE reefs are only known from the lower portions of large layered mafic–ultramafic intrusions (e.g., Bushveld, Great Dyke, and Stillwater). Although PGE reefs have also been found in the upper, more differentiated portions of layered intrusions (e.g., Skaergaard, Rincon del Tigre, Koitelainen, Rio Jacare, Coldwell Complex, Nuasahi, Sonju Lake and Jameson), these are currently all uneconomic. However, the Stella reef is richer in PGE than these examples.

The formation of Stella-type reefs may be favored by tholeiitic intrusions that crystallised along a Fenner trend of differentiation and remained uncontaminated during ascent and crystallization. We suggest that it may be worthwhile to reinvestigate many of these intrusions, particularly where previous analytical programs were widely spaced and/or did not include PGE.

Stella-type reefs are relatively sulfide-poor, and the peak mineralization is commonly located below the peak sulfide occurrence (as also seen at Sonju Lake and Koitelainen). As a result, the mineralization may be difficult to detect macroscopically, and detailed sampling and analysis may be necessary. Barnes (1990) and Maier and Barnes (2005) have shown that Cu/Pd ratios are a useful tool to pinpoint the stratigraphic level of PGE reefs in layered intrusions. The method is based on the relatively more chalcophile behavior, and thus efficient scavenging by sulfide melt, of Pd than Cu, resulting in sharply elevated Cu/Pd ratios above PGE reefs.

The lessons from Stella are that high grade PGE reefs may occur in the upper portions of intrusions if initial sulfide saturation is delayed. This may possibly be facilitated in magmas that evolve along a trend of strong Fe enrichment, such as high-Al tholeiites (Scoates and Mitchell 2000; Ripley and Li 2013) and Archean Fe-rich tholeiites. However, whether any PGE reef in the upper portions of intrusions will be economic remains to be seen. A challenge for many of the known examples could be that they may be relatively strongly affected by S and metal mobility, due to the relatively high volatile content of evolved magma.

Conclusions

The Stella intrusion hosts one of the richest PGE mineralizations known on Earth. The mineralization is unusual in that it is located in the upper portion of the intrusion, consisting of interlayered magnetitite and anorthosite–leucogabbro. Much of the interval is relatively sulfide poor (< 500 ppm S) but contains abundant PGM, mainly antimonides and arsenides, which are typically hosted by silicates rather than sulfides or oxides. The sulfides comprise approximately equal proportions of chalcopyrite and pyrite.

We propose that the reefs formed through a complex sequence of events. The proto cumulate assemblage consisted of magnetite leucogabbro hosting semi-massive magnetite layers and magmatic sulfides enriched in PGE, Cu, and TABS. The sulfides likely formed in response to Fe depletion of the magma following the appearance of magnetite on the liquidus. Ascending deuteric and metamorphic country rock fluids, the latter enriched in As, Sb, and Bi were trapped beneath relatively impermeable magnetite cumulate layers. The fluids mobilized S, Cu, Au, Se, Bi, and Te from the lower portion of the mineralized interval, whereas PGE were stabilized by As and Sb to form PGM.

The relative paucity of S may render Stella-type reefs difficult to identify megascopically. Furthermore, the upper magnetite-rich portions of layered intrusions have, in the past, been poorly studied with regard to possible PGE mineralization. Therefore, important reef-type PGE mineralization may have been overlooked.

Supplementary Information The online version contains supplementary material available at https://doi.org/10.1007/s00126-023-01189-5.

Acknowledgments Harmony Gold Mining Company Limited permitted access to their properties and provided the samples and invaluable logistic support. The authors thank Tony Oldroyd for making the thin sections and Duncan Muir for assisting in the processing of the element maps.

Author contributions WDM conceived the project and collected the samples. SJB conducted the analyses and provided input to discussions and data interpretations. WDS provided input to discussions and data interpretation.

Funding University of Pretoria provided a generous funding. Additional funding was received from NSERC (to SJB). The samples were collected in 2002 while WDM was working at the University of Pretoria who provided generous funding.

Declarations

Competing interest There are no competing interests.

Open Access This article is licensed under a Creative Commons Attribution 4.0 International License, which permits use, sharing, adaptation, distribution and reproduction in any medium or format, as long as you give appropriate credit to the original author(s) and the source, provide a link to the Creative Commons licence, and indicate if changes were made. The images or other third party material in this article are included in the article's Creative Commons licence, unless indicated otherwise in a credit line to the material. If material is not included in the article's Creative Commons licence and your intended use is not permitted by statutory regulation or exceeds the permitted use, you will need to obtain permission directly from the copyright holder. To view a copy of this licence, visit http://creativecommons.org/licenses/by/4.0/.

References

Anderson JC, Rasmussen H, Nielsen TFD, Ronsbo JG (1998) The Triple Group and the Platinova Au and Pd reefs in the Skaergaard intrusion: stratigraphic and petrographic relations. Econ Geol 93:485–509

Andrews G (2002) Platinum-group element mineralization in the Stella layered intrusion, Kraaipan greenstone belt. Unpubl. MSc dissertation. Rhodes University, South Africa, p 115

Anhaeusser CR, Walraven F (1999) Episodic granitoid emplacement in the western Kaapvaal Craton: evidence from the Archaean Kraaipan granite-greenstone terrane, South Africa. J Afr Earth Sci 8:289e309

Ballhaus CG, Stumpfl EF (1986) Sulphide and platinum mineralization in the Merensky Reef: evidence from hydrous silicates and fluid inclusions. Contrib Mineral Petrol 94:193–204

Barnes S-J (1990) The use of metal ratios in prospecting for platinum-group element deposits in mafic and ultramafic intrusions. J Geochem Exp 37:91–99

Barnes S-J (2016). Chalcophile elements. In: White WM (ed) Encyclopedia of geochemistry. https://doi.org/10.1007/978-3-319-39193-9_220-1

Barnes SJ, Mansur ET (2022) Distribution of Te, As, Bi, Sb, and Se in mid-ocean ridgebasalt and komatiites and in picrites and basalts from large igneous provinces: implications for the formation of magmatic Ni-Cu-platinum group element deposits. Econ Geol 117:1919–1933

Barnes SJ, Keays RR, Hoatson DM (1992) Distribution of sulfides and PGE within the porphyritic websterite zone of the Munni Complex, Western Australia. Aust J Earth Sci 39:289–351

Barnes S-J, Savard D, Bédard LP, Maier WD (2009) Selenium and sulfur concentrations in the Bushveld Complex of South Africa and implications for formation of the platinum-group element deposits. Mineralium Deposita 44:647–663

Barrie CT, MacTavish AD, Walford PC, Chataway R, Middaugh R (2002) Contact-type and magnetitite reef-type Pd-Cu mineralization in ferroan olivine gabbros of the Coldwell Complex, Ontario. In: Cabri LJ (ed) The geology, geochemistry, mineralogy and mineral beneficiation of platinum-group elements, Can Inst Min Metall Petrol, Spec Vol, vol 54, pp 321–338

Bédard JH (2006) Trace element partitioning in plagioclase feldspar. Geochimica et Cosmochimica Acta 70:3717–3742

Bird DK, Brooks CK, Gannicott RA, Turner PA (1991) A gold-bearing horizon in the Skaergaard intrusion, East Greenland. Econ Geol 86:1083–1092

Boucher A, Mathieu L, Hamilton MA, Bedeaux P, Daigneault R (2021) Petrogenesis and economic potential of the Obatogamau Formation, Chibougamau area, Abitibi greenstone belt. Canad J Earth Sci 58(6):519–541

Boudreau AE, McCallum IS (1992) Concentration of platinum-group elements by magmatic fluids in layered intrusions. Econ Geol 87:1830–1848

Bowen NL (1917) The problem of the anorthosites. J Geol 25(3):209–243

Cawthorn RG, Ashwal LD (2009) Origin of anorthosite and magnetite layers in the Bushveld Complex, constrained by major element compositions of plagioclase. J Petrol 50:1607–1637

Dare SA, Barnes S-J, Beaudoin G (2012) Variation in trace element content of magnetite crystallized from a fractionating sulfide crystal-liquid, Sudbury, Canada: implications for provenance discrimination. Geochimica et Cosmochimica Acta 88:27–50

Dijon MLN, Barnes S-J (2012) Changes in sulfides and platinum-group minerals with the degree of alteration in the Roby, Twilight, and high grade zones of the Lac des Iles Complex, Ontario. Canada. Mineralium Deposita 47(8):875–896

Duchesne JC (1999) Fe-Ti deposits in Rogaland anorthosites (South Norway): geochemical characteristics and problems of interpretation. Mineral Deposita 34:182–198

Eckstrand OR, Grinenko LN, Krouse HR, Paktunc AD, Schwann PL, Scoates RF (1989) Preliminary data on sulphur isotopes and Se/S ratios, and the source of sulphur in magmatic sulphur in magmatic sulphides from the Fox River Sill, Molson Dykes and Thompson nickel deposits, northern Manitoba. Curr Rese Part C. Geol Surv Can 89–1C:235–242

Eckstrand OR, Hulbert LJ (1987) Selenium and the source of sulfur in magmatic nickel and platinum deposits [abs.]. Geological Association of Canada-Mineralogical Association of Canada program with abstracts, vol 12. p 40

Ewart A, Griffin WL (1994) Application of proton-microprobe data to trace-element partitioning in volcanic rocks. Chem Geol 117(1-4):251–284

Forien M, Tremblay J, Barnes S-J, Burgisser A, Page P (2015) The role of viscous particle segregation in forming chromite layers from slumped crystal slurries: insights from analogue experiments. J Petrol 56:2425–2444

Fuchs WA, Rose AW (1974) The geochemical behavior of platinum and palladium in the weathering cycle in the Stillwater Complex, Montana. Econ Geol 69(3):332–346

Gumsley A, Stamsnijder J, Larsson E, Söderlund U, Naeraa T, De Kock M, Sałacińska A, Gawęda A, Humbert F, Ernst R (2020) Neoarchean large igneous provinces on the Kaapvaal Craton in southern Africa re-define the formation of the Ventersdorp Supergroup and its temporal equivalents. GSA Bulletin 132(9-10):1829–1844

Hammond NQ, Moore JM (2006) Archaean lode gold mineralisation in banded iron formation at the Kalahari Goldridge deposit, Kraaipan Greenstone Belt, South Africa. Mineral Deposita 41:483–503

Hauck SA, Severson MJ, Zanko L, Barnes S-J, Morton P, Alminas H, Foord EE, Dahlberg EH (1997) An overview of the geology and oxide, sulphide, and platinum-group element mineralization along the western and northern contacts of the Duluth Complex. Geol Soc America Spec Pap 312:137–186

Hey PV (1999) The effects of weathering on the UG2 chromitite reef of the Bushveld Complex, with special reference to the platinum-group minerals. South Afr J Geol 102(3):251–260

Higgins MD (2005) A new interpretation of the structure of the Sept Iles Intrusive suite, Canada. Lithos 83(3-4):199–213

Holwell DA, Adeyemi Z, Ward LA, Smith DJ, Graham SD, McDonald I, Smith JW (2017) Low temperature alteration of magmatic Ni-Cu-PGE sulfides as a source for hydrothermal Ni and PGE ores: a quantitative approach using automated mineralogy. Ore Geol Rev 91:718–740

Junge M, Oberthür T, Kraemer D, Melcher F, Piña R, Derrey IT, Manyeruke T, Strauss H (2019) Distribution of platinum-group elements in pristine and near-surface oxidized Platreef ore and the variation along strike, northern Bushveld Complex, South Africa. Mineralium Deposita 54(6):885–912

Karykowski BT, Polito PA, Maier WD, Gutzmer J, Krause J (2017) New insights into the petrogenesis of the Jameson Range layered intrusion and associated Fe-Ti-PV-PGE-Au mineralisation, West Musgrave Province, Western Australia. Mineral Deposita 52:233–255

Klemm DD, Henckel J, Dehm R, von Gruenewaldt G (1985) The geochemistry of titanomagnetite in magnetite layers and their host rocks of the eastern Bushveld Complex. Econ Geol 80:1075–1088

Latypov R, Chistyakova S, Costin G, Namur O, Barnes S, Kruger W (2020) Monomineralic anorthosites in layered intrusions are indicators of the magma chamber replenishment by plagioclase-only-saturated melts. Sci Rep 10(1):1–14

Li C, Naldrett AJ (1993) Sulfide capacity of magma; a quantitative model and its application to the formation of sulfide ores at Sudbury, Ontario. Econ Geol 88(5):1253–1260

Li C, Boudreau AE (2017) The origin of high-Cu/S sulfides by shallow-level degassing in the Skaergaard intrusion, East Greenland. Geology 45:1075–1078

Lyubetskaya T, Korenaga J (2007) Chemical composition of Earth's primitive mantle and its variance: 1. Method and results. J Geophys Res: Solid Earth 112(B3)

Maier WD, Barnes S-J (2005) Application of lithogeochemistry to exploration for PGE deposits. Exploration for platinum-group elements deposits. MAC Short Course Ser 35:309–341

Maier WD, Barnes S-J, Gartz V, Andrews G (2003) Pt-Pd reefs in magnetitites of the Stella layered intrusion, South Africa: a world of new exploration opportunities for platinum group elements. Geology 31(10):885–888

Maier WD, Howard HM, Smithies RH, Yang SH, Sarah-Jane Barnes, O'Brien H, Huhma H, Gardoll S (2015) Magmatic ore deposits in mafic-ultramafic intrusions of the Giles event, Western Australia. Ore Geol Rev 71:405–436

Maier WD, Barnes S-J, Muir D, Savard D, Lahaye Y, Smith WD (2021) Formation of Bushveld anorthosite by reactive porous flow. Contrib Mineral Petrol 176(1):1–12

Mansur E, Barnes S-J, Ferreira Filho CF (2021) The effects of post-cumulus alteration on the distribution of chalcophile elements in magmatic sulfide deposits and implications for the formation of low-S-high-PGE zones: the Luanga deposit, Carajás Mineral Province, Brazil. Canad Mineral 59(6):1453–1484

Mansur ET, Barnes S-J (2020) Concentrations of Te, As, Bi, Sb and Se in the Marginal Zone of the Bushveld Complex: evidence for crustal contamination and the nature of the magma that formed the Merensky Reef. Lithos 358:105407

Mansur ET, Barnes SJ, Savard D, Webb PC (2020) Determination of Te, As, Bi, Sb and Se (TABS) in geological reference materials and GeoPT proficiency test materials by hydride generation-atomic fluorescence spectrometry (HG-AFS). Geostand Geoanal Res 44(1):147–167

Meurer WP, Klaber S, Boudreau AE (1997) Discordant bodies from olivine-bearing zones III and IV of the Stillwater Complex, Montana–evidence for postcumulus fluid migration and reaction in layered intrusions. Contrib Mineral Petrol 130(1):81–92

Miller JD Jr (1999) Geochemical evaluation of platinum-group element (PGE) mineralization in the Sonju Lake intrusion, Finland, Minnesota. Minnesota Geoogical Survey Inform Circular 44:32

Mokchah N, Mathieu L (2022) Origin and evolution of the iron-rich upper unit and Fe–Ti–V mineralization of the Neoarchean Lac Doré layered intrusion, Chibougamau, Québec. J Petrol 63(3):egac006

Morse SA (1981) Kiglapait geochemistry IV: the major elements. Geochim et Cosmochim Acta 45:461–479

Mountain BW, Wood SA (1988) Chemical controls on the solubility, transport and deposition of platinum and palladium in hydrothermal solutions; a thermodynamic approach. Econ Geol 83(3):492–510

Mutanen T (1989) Koitelainen intrusion and Kevitsa - Satovaara Complex. Geol Surv Finland Guide 28:49

Naldrett AJ (2004) Magmatic sulfide deposits: geology, geochemistry and exploration. Springer Science & Business Media

Namur O, Charlier B, Toplis MJ, Higgins MD, Hounsell V, Liégeois JP, Vander Auwera J (2011) Differentiation of tholeiitic basalt to A-type granite in the Sept Iles layered intrusion, Canada. J Petrol 52(3):487–539

Oberthür T, Cabri LJ (2002) Platinum-group element mineralization of the Great Dyke, Zimbabwe. Geol Geochem Mineral Min Beneficiation Platinum-Group Elements 54:793–810

Oberthür T, Melcher F, Buchholz P, Locmelis M (2013) The oxidized ores of the Main Sulphide Zone, Great Dyke, Zimbabwe: turning resources into minable reserves-mineralogy is the key. J Southern Afr Inst Min Metallurgy 113(3):00–00

Otamendi JE, Tiepolo M, Walker BA Jr, Cristofolini EA, Tibaldi AM (2016) Trace elements in minerals from mafic and ultramafic cumulates of the central Sierra de Valle Fértil, Famatinian arc, Argentina. Lithos 240:355–370

Polivchuk M (2018) The formation of vanadium deposits in the Archean Rivière Bell Complex, Quebec: insights from Fe-Ti oxide chemistry (Doctoral dissertation,. Université d'Ottawa/University of Ottawa)

Prendergast MD (1998) Platinum exploration in the Rincon del Tigre Complex, eastern Bolivia. Trans Inst Min Metall B 107:39–47

Prichard HM, Mondal SK, Mukherjee R, Fisher PC, Giles N (2018) Geochemistry and mineralogy of Pd in the magnetitite layer within the upper gabbro of the Mesoarchean Nuasahi Massif (Orissa, India). Mineralium Deposita 53(4):547–564

Queffurus M, Barnes S-J (2015) A review of sulfur to selenium ratios in magmatic nickel–copper and platinum-group element deposits. Ore Geol Rev 69:301–324

Ramotoroko CD, Ranganai RT, Nyabeze P (2016) Extension of the Archaean Madibe-Kraaipan granite-greenstone terrane in south-east Botswana: constraints from gravity and magnetic data. J Afr Earth Sci 123:39–56

Ripley EM, Li C (2013) Sulfide saturation in mafic magmas: is external sulfur required for magmatic Ni-Cu-(PGE) ore genesis? Econ Geol 108(1):45–58

Rudnick RL, Fountain DM (1995) Nature and composition of the continental crust: a lower crustal perspective. Rev Geophys 33(3):267–309

Sá HS, Barnes S-J, Prichard HM, Fisher PC (2005) The distribution of base metals and platinum-group elements in magnetitites and their host rocks in the Rio Jacaré intrusion, Northeastern Brazil. Econ Geol 100:333–348

Schiffries CM (1982) The petrogenesis of a platiniferous dunite pipe in the Bushveld complex; infiltration metasomatism by a chloride solution. Econ Geol 77(6):1439–1453

Schmitz MD, Bowring SA, de Wit MJ, Gartz V (2004) Subduction and terrane collision stabilize the western Kaapvaal craton tectosphere 2.9 billion years ago. Earth Planet Sci Lett 222(2):363–376

Scoates JS, Mitchell JN (2000) The evolution of troctolitic and high-Al basaltic magmas in Proterozoic anorthosite plutonic suites and implications for the Voisey's Bay massive Ni-Cu sulphide deposit. Econ Geol 95:677–701

Sluzhenikin SF, Yudovskaya MA, Barnes SJ, Abramova VD, Le Vaillant M, Petrenko DB, Grigor'eva AV, Brovchenko VD (2020) Low-sulfide platinum group element ores of the Norilsk-Talnakh camp. Econ Geol 115(6):1267–1303

Smith PM, Asimow PD (2005) Adiabat_1ph: a new public front-end to the MELTS, pMELTS, and pHMELTS models. Geochem Geophys Geosyst 6(2)

Smith WD, Maier WD (2021) The geotectonic setting, age and mineral deposit inventory of global layered intrusions. Earth-Sci Rev 220:103736

Smith WD, Maier WD, Barnes SJ, Moorhead G, Reid D, Karykowski B (2021) Element mapping the Merensky Reef of the Bushveld Complex. Geosci Front 12(3):101101

Song XY, Qi HW, Hu RZ, Chen LM, Yu SY, Zhang JF (2013) Formation of thick stratiform Fe-Ti oxide layers in layered intrusion and frequent replenishment of fractionated mafic magma: evidence from the Panzhihua intrusion, SW China. Geochem Geophys Geosyst 14(3):712–732

Sullivan NA, Zajacz Z, Brenan JM, Tsay A (2022) The solubility of platinum in magmatic brines: insights into the mobility of PGE in ore-forming environments. Geochim et Cosmochim Acta 316:253–272

Sun SS, McDonough WF (1989) Chemical and isotopic systematics of oceanic basalts: implications for mantle composition and processes. Geol Soc London, Special Publications 42(1):313–345

Theal GM (1919) History of South Africa from 1873 to 1884. George Allen & Unwin Ltd., London, p 147f

Toplis MJ, Carroll MR (1995) An experimental study of the influence of oxygen fugacity on Fe-Ti oxide stability, phase relations, and mineral—melt equilibria in ferro-basaltic systems. J Petrol 36(5):1137–1170

Vermaak CF (1976) The Merensky Reef; thoughts on its environment and genesis. Econ Geol 71(7):1270–1298

von Gruenewaldt G (1976) Sulfides in the Upper Zone of the eastern Bushveld Complex. Econ Geol 71:1324–1335

Wilson AH, Murahwi CZ, Coghill BM (2000) The geochemistry of the PGE subzone in the Selukwe Subchamber, Great Dyke: an intra-formational layer model for platinum group element enrichment in layered intrusions. Mineral Petrol 68(1):115–140

Wood SA, Cabri LJ (2002) The aqueous geochemistry of the platinum-group elements with applications to ore deposits. Geol Geochem Mineral Min Benef Platinum-Group Elements 54:211–249

Publisher's note Springer Nature remains neutral with regard to jurisdictional claims in published maps and institutional affiliations.